atmosphere

Article

Accuracy Analysis of Real-Time Precise Point Positioning—Estimated Precipitable Water Vapor under Different Meteorological Conditions: A Case Study in Hong Kong

Ying Xu, Lin Ma, Fangzhao Zhang *, Xin Chen and Zaozao Yang

College of Geodesy and Geomatics, Shandong University of Science and Technology, Qingdao 266590, China; yingxu@sdust.edu.cn (Y.X.)
* Correspondence: fzzhang@sdust.edu.cn

Abstract: Precipitable water vapor (PWV) monitoring with real-time precise point positioning (PPP) is required for the improved early detection of increasingly common extreme weather occurrences. This study takes Hong Kong as the research object. The aim is to explore the accuracy of real-time global navigation satellite system (GNSS) PPP in estimating PWV at low latitudes and under different weather conditions. In this paper, real-time PPP is realized by using observation data from continuously operating reference stations (CORS) in Hong Kong and real-time products from the Centre National d'Etudes Spatiales (CNES). The Tm model calculated using numerical weather prediction (NWP) data converts the zenith tropospheric delay (ZTD) of real-time PPP inversion into PWV and evaluates its accuracy using postprocessing products. The experimental results show that compared with GPS, multi-GNSS can reduce the convergence time of PPP by 29.20% during rainfall periods and by 12.06% during nonrainfall periods. The improvement in positioning accuracy is not obvious, and the positioning accuracy of the two is equivalent. Real-time PPP ZTD experiments show that there are lower average values for bias, standard deviation (STDEV), and root mean square (RMS) during nonrainfall periods than during rainfall periods. Real-time PPP PWV experiments show that there are also lower bias, STDEV, and RMS values during nonrainfall periods than during rainfall periods. The comparative study between rainfall and nonrainfall periods is of great significance for the real-time monitoring and forecasting of water vapor changes.

Keywords: GNSS; real-time PPP; ZTD; PWV; NWP

Citation: Xu, Y.; Ma, L.; Zhang, F.; Chen, X.; Yang, Z. Accuracy Analysis of Real-Time Precise Point Positioning—Estimated Precipitable Water Vapor under Different Meteorological Conditions: A Case Study in Hong Kong. *Atmosphere* **2023**, *14*, 650. https://doi.org/10.3390/atmos14040650

Academic Editor: Tomeu Rigo

Received: 28 February 2023
Revised: 28 March 2023
Accepted: 29 March 2023
Published: 30 March 2023

1. Introduction

The function of water vapor in atmospheric circulation and climate change is significant. Many meteorological phenomena are linked to precipitable water vapor (PWV). Monitoring water vapor in real time is crucial for weather forecasting and severe weather alerts. In 1992, Bevis proposed, for the first time, a system using global navigation satellite system technology to retrieve atmospheric PWV (GNSS PWV) [1]. Since then, the retrieval of PWV through GNSS technology has garnered the interest of several academics [2,3]. The advantages of GNSS technology include high accuracy, high spatial and temporal resolution, all-weather monitoring, cheap cost, etc., in comparison to the conventional methods of PWV observation (e.g., microwave radiation and radiosonde). Thus, it is frequently used for weather monitoring and forecasting [4–7].

Precise point positioning (PPP) offers more computing efficiency as well as operational and implementation simplicity compared to relative positioning. Through various error correction and parameter estimates, PPP technology enables high-precision GNSS positioning technology to be obtained for any point location on Earth by using single-station receivers and precise orbit and clock error data based on combined carrying phase and pseudorange observation values [8,9]. In recent years, with the rapid construction and development of GPS, GLONASS, BDS, Galileo, and other systems, multisystem GNSS (multi-GNSS) data processing and associated applications have become the focus of development trends in GNSS technology. On the other hand, multi-GNSS has the potential to improve GNSS positioning accuracy and dependability by supplying more readily visible satellites, an improved geometric structure of satellite constellations, and more frequencies and signals [10,11]. Jin et al. reviewed the performance, availability, modernization, and hybridization of multi-GNSS [12]. Cai et al. derived the function model and stochastic model of GPS/GLONASS PPP in detail. The results of static examples show that the addition of GLONASS observations can significantly accelerate the convergence speed of positioning solutions, but the improvement in positioning accuracy is not obvious. The kinematic example shows that the positioning accuracy of the three components (east, north, and up) can be improved by more than 50% by adding GLONASS observations [13]. Lou and Liu investigated the GPS/GLONASS/BDS/Galileo combined PPP model, and analyzed the positioning performance of various systems, to validate the positioning performance of multi-GNSS fusion. The results demonstrated that PPP's positioning performance and reliability may benefit greatly from the incorporation of multisystem observations. The convergence speed of PPP may be greatly improved by including multi-GNSS observations in addition to single GPS PPP [14,15]. A lack of studies on multi-GNSS PPP at low latitudes represents a major gap in the above research. Most studies focus on mid-high latitudes or address the worldwide distribution. PPP technology can estimate the absolute zenith tropospheric delay (ZTD) of a station. Delivery of real-time tropospheric products is a key consideration for the use of PPP technology in meteorology [8].

The International GNSS Service Real-time Pilot Project's (IGS RTPP) quick development can keep up with the needs of real-time tropospheric products. For ZTD or PWV retrieval in real time, Li and Yuan relied on GPS PPP. Millimeter-level accuracy is possible when referencing meteorological data or the results of postprocessing [16,17]. Lu and Pan et al. carried out real-time four-constellation integrated PPP ZTD retrieval research. Compared with the pure GPS PPP solution, the ZTD estimation of the four-constellation integrated PPP solution demonstrates a certain improvement in initialization time and accuracy [18,19]. Askne's theory deduces the relationship between ZTD and PWV, providing a theoretical framework for the retrieval of PWV by GNSS [20]. Gendt demonstrated the viability of GNSS PWV [21]. Rocken proved that PWV based on GPS has high accuracy [22]. Yuan examined the precision of real-time GPS PPP PWV retrieval using real-time data from 20 sites throughout the globe. The results show that the accuracy of real-time GPS PPP PWV is better than 3 mm [19]. Li conducted real-time GNSS water vapor experiments with GPS, BDS, Galileo, and GLONASS. The findings demonstrate that the real-time water vapor retrieval of multi-GNSS achieves millimeter-level accuracy and high dependability, which is advantageous for atmospheric detection systems, particularly those used in meteorological applications. PWV based on the retrieval of real-time GNSS data may play a significant role in several domains, including weather monitoring and catastrophe warning [23]. However, most of the above studies were carried out under a single weather condition, and there are relatively few studies on the accuracy evaluation of PPP inversion ZTD and ZTD conversion to PWV under different weather conditions.

This paper uses observation data from Hong Kong continuously operating reference stations (HK CORS) from June 2021 (DOY 173-DOY 179) and August 2021 (DOY 229-DOY 235) to study and analyze the accuracy of real-time PPP estimation of ZTD and PWV under different weather conditions, with the goal of evaluating its performance in low-latitude areas during varying weather conditions (rainfall and nonrainfall). Before obtaining the overall tropospheric delay through parameter estimation, real-time PPP is utilized for data processing. This is the method used to retrieve PWV. The GNSS and meteorological stations in Hong Kong were measured and analyzed. Utilizing Hong Kong radiosonde (RS) data as a reference, the approach was tested, and its accuracy was assessed using the IGS's final product and the PWV results.

This paper is organized as follows: The experimental dataset is provided in Section 2, and the PPP technique for calculating ZTD and converting ZTD to PWV is shown. The positioning performance of real-time PPP is examined in Section 3, along with the precision with which PPP estimates ZTD and with which ZTD is converted into PWV. We discuss the accuracy of PWV in Section 4. Section 5 discusses "Limitations and Future Direction of the Research". Section 6 provides a summary of the experiment's conclusion.

2. Materials and Methods

In order to analyze the positioning performance of real-time PPP and the accuracy of PWV inversion under different weather conditions, this paper collected GNSS observation data in Hong Kong during June (DOY 173-DOY 179) and August (DOY 229-DOY 235) 2021, real-time products provided by the Centre National d'Etudes Spatiales (CNES), troposphere products from the IGS Center, radiosonde PWV (RS PWV) data provided by the National Climate Data Center (NCDC), and the ERA5 reanalysis dataset. The data processing procedure of this paper is shown in Figure 1.

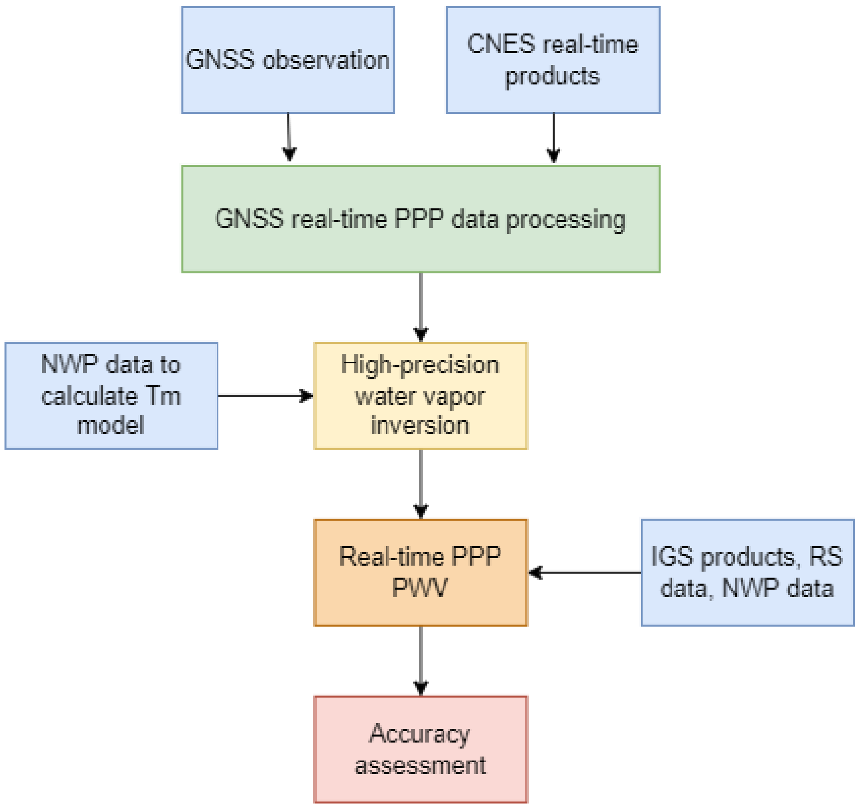

Figure 1. GNSS station real-time atmospheric water vapor inversion process.

2.1. Data Sources

Observation data from 18 GNSS CORS in Hong Kong, China, during June 2021 (DOY 173-DOY 179) and August 2021 (DOY 229-DOY 235) were selected. The data download website is: https://www.geodetic.gov.hk (accessed on 14 September 2022). The location distribution map of the selected stations is shown in Figure 2. The coordinates list of Hong Kong CORS is shown in Table 1.

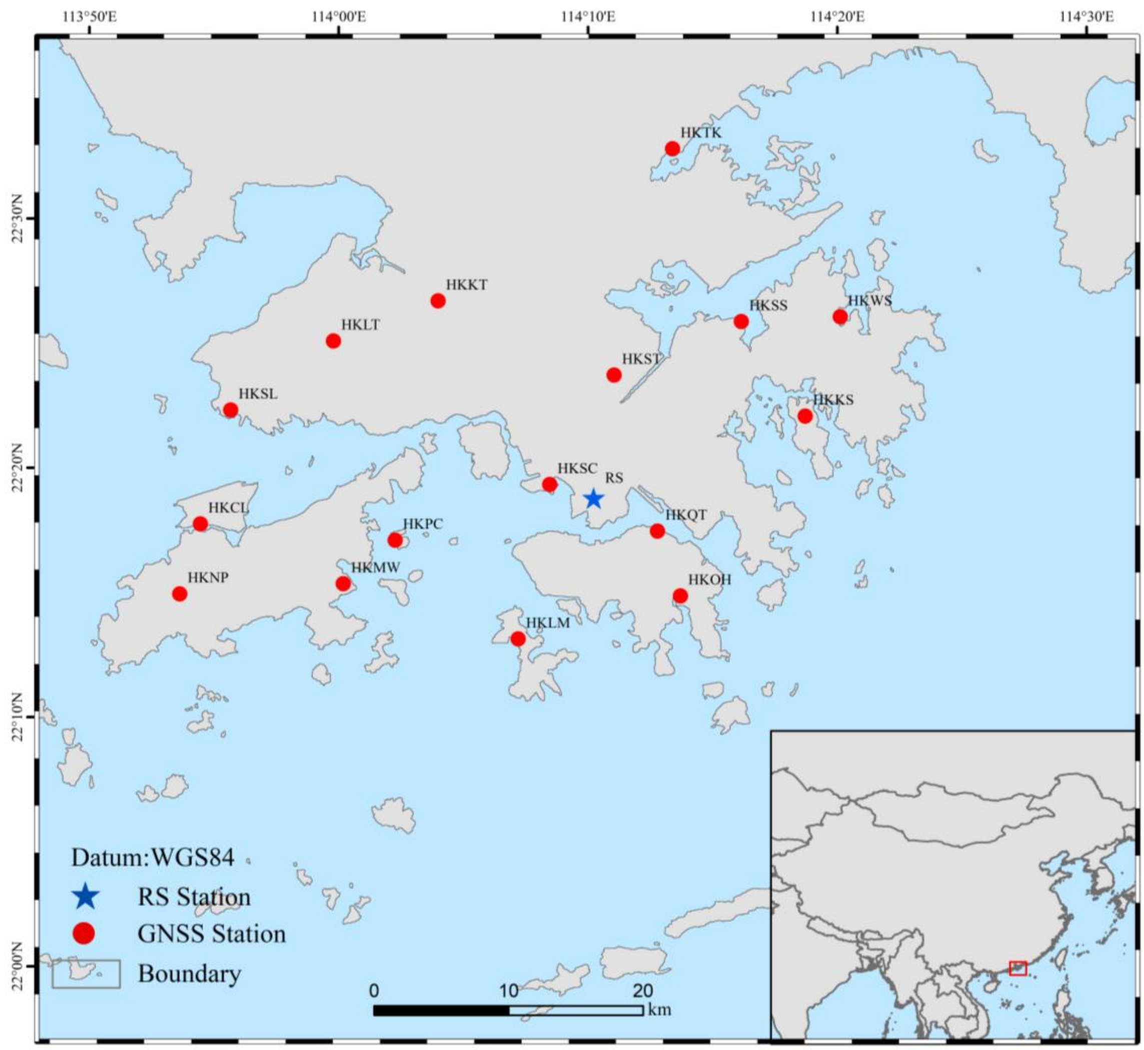

Figure 2. GNSS station and RS station position distribution map.

Table 1. Hong Kong CORS coordinates list.

Station	Latitude (°)	Longitude (°)	Antenna
HKCL	22.2958	113.9077	TRM59800.00
HKFN	22.4946	114.1381	LEIAT504
HKKT	22.3678	114.3119	TRM59800.00
HKKS	22.4449	114.0665	LEIAR25.R4
HKLM	22.2189	114.1200	TRM59800.00
HKLT	22.4181	113.9966	LEIAR25.R4
HKMW	22.2558	114.0031	LEIAR25.R4
HKNP	22.2490	113.8938	LEIAR25.R4
HKOH	22.2476	114.2285	LEIAR25.R4
HKPC	22.2849	114.0378	LEIAR25.R4
HKQT	22.2910	114.2132	TRM59800.00
HKSC	22.3222	114.1411	LEIAR25.R4
HKSL	22.3720	113.9279	LEIAR25.R4
HKSS	22.4310	114.2693	LEIAR25.R4
HKST	22.3952	114.1842	LEIAR25.R4
HKTK	22.5465	114.2232	TRM59800.00
HKWS	22.4342	114.3353	LEIAR25.R4
T430	22.4947	114.1382	TRM59800.00

Because the IGS final product has a delay of about 12~18 weeks, the IGS fast product also has a delay of about 17~41 h, which generally leads to the PPP adopting the post-processing mode. Real-time PPP can also be implemented using the prediction part of IGS ultra-fast products, but its accuracy decreases as the prediction time increases, and real-time PPP implemented in this way has poor performance. The IGS RTPP was officially released in 2013, providing real-time services using real-time products formed by hundreds of real-time tracking stations around the world [24]. At present, several analysis centers can provide real-time service (RTS) products, but most of them only support single GPS systems or dual GPS/GLONASS systems. The RTS products provided by CNES can support four GNSS systems (GPS, GLONASS, Galileo, and BDS), so this paper uses its products for analysis. Real-time CNT products released by CNES can be downloaded from http://www.ppp-wizard.net/products/REAL_TIME (accessed on 14 September 2022); the website can provide sp3/clock products with a sampling rate of 5 min, and the file is named cntwwwwd.sp3/clk. In addition, it also provides a high-sampling-rate clock product with a sampling rate of 5 s. The acquisition delay of both files is 1 d [25].

The radiosonde data were from the Integrated Global Radiosonde Archive Version 2 (IGRA2) dataset generated by the National Climate Data Center of the United States in August 2016. The location distribution is shown in Figure 2. The experiment used radiosonde data from June 2021 (DOY 173-DOY 179) and August 2021 (DOY 229-DOY 235). The PWV of the radiosonde station was used to evaluate the accuracy of real-time PPP PWV. The PWV data of the radiosonde station were updated twice a day at 08:00 (UTC 00:00) and 20:00 (UTC 12:00). Data download address: ftp://ftp.ncdc.noaa.gov/pub/data/igra/derived/derived-Por (accessed on 18 September 2022) [26]. The ERA5 pressure stratification and single-layer data were derived from the ERA5 reanalysis dataset provided by the European Centre for Medium-Range Weather Forecasts (ECMWF).

The experiment collected the ERA5 pressure stratification data during June 2021 (DOY 173-DOY 179) and August 2021 (DOY 229-DOY 235) to generate Tm and converted the ZTD of real-time PPP inversion into PWV. The horizontal resolution of ERA5 reanalysis data was $0.25^\circ \times 0.25^\circ$, the temporal resolution was 1 h, and the vertical stratification was divided into 37 layers. Data download address: https://www.ecmwf.int (accessed on 18 September 2022). GNSS ZTD data were sourced from the IGS Center. This paper used ZTD data from June 2021 (DOY 173-DOY 179) and August 2021 (DOY 229-DOY 235) [27]. The selected stations are shown in Figure 2, where stations HKSL and HKWS are IGS stations.

2.2. Data Processing Method

In this paper, 18 GNSS observation stations in Hong Kong were selected for real-time PPP data processing to explore the positioning performance of real-time PPP and the accuracy of water vapor inversion. IGS ZTD and radiosonde station PWV were used as references to evaluate the accuracy of real-time PPP ZTD and real-time PPP PWV. The average values of bias, standard deviation (STDEV), and root mean square (RMS) were used as precision evaluation indexes.

2.2.1. PPP Functional Model

In PPP algorithm processing, real-time orbit and clock products provided by CNES are used to produce high-precision solutions based on dual-frequency combined observations. The ionospheric delay in the observations is eliminated by using dual-frequency ionosphere-free (IF) combination observations, while the tropospheric delay error is estimated by introducing parameters. The conventional PPP IF combination observation model is shown in Equations (1) and (2) [28], and the ZTD of the station can be extracted according to Equations (1) and (2):

$$P_{IF}^{s} = \rho_r^s + c \cdot (dt_r + dt^s) + M_{wet} \cdot ZWD + \varepsilon_{P,IF} \tag{1}$$

$$L_{IF}^{s} = \rho_r^s + c \cdot (dt_r + dt^s) + M_{wet} \cdot ZWD + B_{IF} + \varepsilon_{L,IF} \tag{2}$$

where $B_{IF} = \frac{f_1^2}{f_1^2 - f_2^2}\lambda_1 N_1 - \frac{f_2^2}{f_1^2 - f_2^2}\lambda_2 N_2$; indexes r and s refer to the receiver and the satellite; $P^s_{IF,r}$ and $L^s_{IF,r}$ are the IF combination of pseudorange and carrier phase observations, respectively; c denotes light speed; f_i is the frequency; ρ^s_r is the geometrical range between the satellite and the receiver; dt_r and dt^s are receiver clock error and satellite clock error, respectively; M_{wet} is the zenith wet delay (ZWD) mapping function; ZWD is the zenith wet delay at the station and the zenith hydrostatic delay (ZHD) corrected by the model; λ_1 and λ_2 are the wavelengths corresponding to L_1 and L_2, respectively; N_1 and N_2 are the integer ambiguities corresponding to L_1 and L_2, respectively; $\varepsilon_{P,IF,}$ and $\varepsilon_{L,IF}$ are the multipath effects and other unmodeled errors of the pseudorange and carrier phase, respectively.

The observation processing strategy, error correction model, and parameter estimation method used in the PPP solution are shown in Table 2.

Table 2. PPP algorithm processing method.

Observation	Combination of observation	IF
	Elevation mask angle	10°
	Stochastic model	Elevation weighting
Error correction	Phase wrapping	Correction
	Phase center variation	Igs14.atx
	Atmospheric loading	Leave out
	Tide correction	Solid tide, polar tide, and ocean tide
	Relativistic correction	Correction
	Tropospheric delay	Parameter estimation
Parameter estimation	Tropospheric mapping function	NMF
	Site coordinates	Constant
	Station receiver clock error	White noise
	Ambiguity	Float ambiguity
	Filtering method	Extended Kalman filter

2.2.2. PPP PWV Calculation Method

The PPP PWV calculation method is as follows: (1) The Saastamoinen model is used to calculate the station ZHD [29]. (2) ZWD is stripped from the ZTD of real-time PPP inversion. (3) PPP PWV is calculated with ZWD [30].

$$\begin{aligned} ZWD &= ZTD - ZHD \\ &= ZTD - \frac{0.002277 \cdot P}{1 - 0.00266 \cdot \cos(2\varphi) - 0.00028 \cdot H} \end{aligned} \tag{3}$$

$$PWV = \frac{10^6}{\left(K_2' + K_3/T_{\mathrm{m}}\right) \cdot R_V \cdot \rho} \cdot ZWD \tag{4}$$

where P denotes the atmospheric pressure, the unit is hPa; H denotes the geodetic height of the station; K_2',K_3, and R_V are constants, and their values are 16.48 K·hPa^{-1}, (3.776 ± 0.014) × 105 K2·hPa^{-1}, and 461 J·(Kg·K)$^{-1}$; ρ is the water vapor constant; and Tm is the atmospheric weighted temperature. Its mathematical expression is:

$$Tm = \frac{\int_H^{+\infty} \frac{e}{T} dh}{\int_H^{+\infty} \frac{e}{T^2} dh} \tag{5}$$

where e is water vapor pressure and T is absolute temperature, which were obtained from ERA5 data. dh is the increment of the vertical integration path. The horizontal resolution of ERA5 data is 0.25° × 0.25°. After calculating the Tm at the grid point, the Kriging interpolation method was used to interpolate the Tm at the station.

2.2.3. Precision Evaluation Index

In this paper, bias, STDEV, and RMS values are introduced to evaluate the accuracy of PPP inversion ZTD and PWV. The expressions of bias, STDEV, and RMS are as follows:

$$Bias = \frac{\sum_{i=1}^{n}(\triangle x)}{n} \tag{6}$$

$$STDEV = \sqrt{\frac{\sum_{i=1}^{n}\left(\triangle x - \overline{\Delta x}\right)^2}{n}} \tag{7}$$

$$RMS = \sqrt{\frac{\sum_{i=1}^{n}(\triangle x)^2}{n}} \tag{8}$$

where n represents the total number of samples, Δx is the difference between the two sets of data, and $\overline{\Delta x}$ is the average value of the difference between the two sets of data.

3. Results

In order to evaluate the positioning performance of real-time PPP and the accuracy of PPP ZTD during rainfall and nonrainfall periods, observation data from 18 GNSS observation stations in Hong Kong, China, during June 2021 (DOY 173-DOY 179, during rainfall) and August 2021 (DOY 229-DOY 235, during nonrainfall) were selected. The real-time PPP data processing was carried out by using the real-time orbit and real-time clock products provided by CNES and the RTKLIB open-source software platform. The positioning accuracy of real-time PPP was evaluated by comparing it with the final product of IGS. Then, the real-time PPP PWV of the HKSC station was obtained by using the *Tm* model established by the ERA5 dataset, and the PWV of the radiosonde station was used as a reference to evaluate the accuracy of real-time PPP PWV.

3.1. Real-Time Static PPP Accuracy Analysis

In the process of PPP, if there is no perceptible change in the position of the point to be determined, it can be ignored for a period. Therefore, in data processing, the coordinates of the point to be determined can be considered as a fixed set of constants, called static PPP; otherwise, they are referred to as kinematic PPP. Since the coordinates of the point to be determined can be considered as a set of constants, the positioning accuracy of static PPP is higher than that of kinematic PPP. Therefore, static PPP was used in this paper. Since HKSL and HKWS stations in Hong Kong are IGS stations, the station coordinates products published by IGS were used as reference truth values, and HKSL and HKWS stations were used as examples to evaluate their positioning accuracy. When the absolute values of the three directions of E, N, and U were less than 10 cm and were less than 10 cm in the subsequent 20 consecutive epochs, the direction was considered to converge. The positioning error after convergence was calculated to evaluate the accuracy of the real-time PPP static solution.

Figure 3a shows the error distribution of real-time GPS PPP at HKSL and HKWS stations. Table 3 shows the RMS and average convergence time of the real-time GPS PPP error at each station. According to Figure 3a, the positioning accuracy of HKSL and HKWS in the U direction of DOY 175 during the rainfall period was about 6 cm, and the positioning accuracy of E, N, and U directions for other days was better than 5 cm. The overall positioning error of the two stations was relatively stable with time. Errors in the E direction of DOY 173 and the U direction of DOY 175 fluctuated greatly, which may have been caused by the unstable atmospheric environment during rainfall. During the nonrainfall period, except for the large fluctuation in the U direction in DOY 231, the overall positioning errors in the E, N, and U directions were relatively stable. Table 3 shows the RMS and convergence time of HKSL and HKWS during rainfall and nonrainfall periods. The results show that the two stations had larger RMS values and longer convergence times during rainfall. During rainfall periods with large positioning errors and convergence times, the average positioning accuracy of real-time static GPS PPP in the E, N, and U directions was 1.69 cm, 0.80 cm, and 2.37 cm, respectively, and the average convergence time was 62.50 min. This shows that the convergent GPS PPP can maintain high positioning accuracy and reliability in the three directions of E, N, and U, and the disadvantage is that the convergence time is longer.

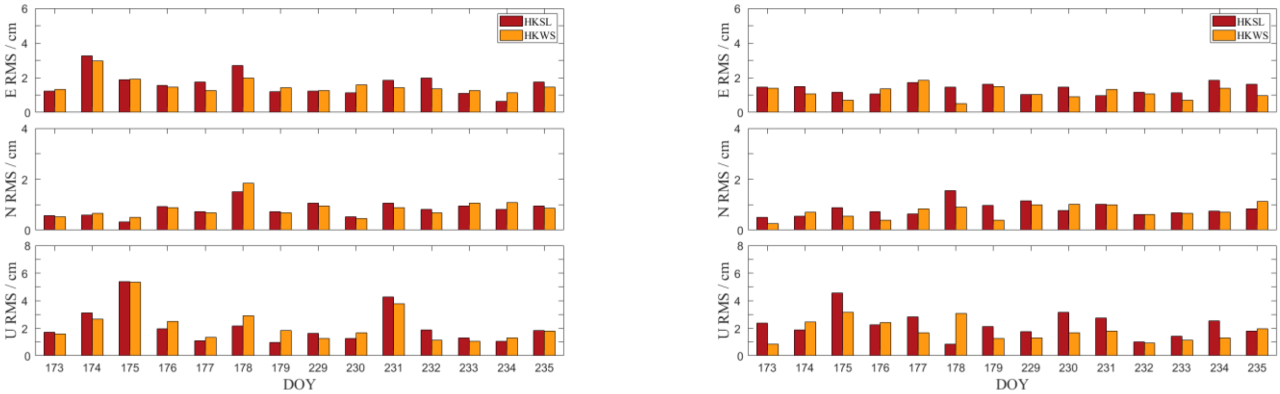

(**a**) (**b**)

Figure 3. (**a**) Real-time static GPS PPP error; (**b**) Real-time static multi-GNSS PPP error.

Table 3. Real-time GPS PPP error and convergence time.

Station	E (cm)	N (cm)	U (cm)	Convergence Time (min)	E (cm)	N (cm)	U (cm)	Convergence Time (min)
	During Rainfall				During Nonrainfall			
HKSL	1.94	0.77	2.34	47	1.38	0.88	1.88	37.5
HKWS	1.43	0.83	2.4	78	1.31	0.83	2.06	33

To study the changes in real-time GPS PPP accuracy and convergence time after adding GLONASS, BDS, and Galileo observations, in this section, real-time CNES products are also used for real-time multisystem (GPS/GLONASS/BDS/Galileo) PPP data processing. Figure 3b shows the error distribution of real-time multisystem PPP in each station after convergence. Table 4 shows the RMS and average convergence time of the real-time multisystem PPP error of each station. As can be seen from Figure 3b, the overall accuracy of the two stations in the E and N directions was improved, and the error of the HKWS station in the E direction in DOY 174 was reduced from 3.25 cm to 1.49 cm. The statistical results in Table 4 show that the average positioning accuracy of the real-time static multisystem combination in the E, N, and U directions during rainfall was 1.48 cm, 0.7 cm, and 2.36 cm, respectively, and the average convergence time was 44.25 min. Compared with real-time GPS PPP, the positioning accuracy of real-time multisystem PPP in the E direction and the N direction was improved by about 11.38% and 5.43%, respectively, and the accuracy in the U direction was maintained. Compared with GPS, the convergence time of real-time multi-GNSS PPP was reduced by 29.20% and 12.06% during rainfall and nonrainfall periods, respectively. This shows that the introduction of real-time GLONASS/BDS/Galileo multisystem PPP can effectively improve the convergence speed of real-time PPP and improve the overall positioning accuracy of real-time GPS PPP.

Table 4. Positioning error and convergence time of real-time multi-GNSS PPP.

Station	E (cm)	N (cm)	U (cm)	Convergence Time (min)	E (cm)	N (cm)	U (cm)	Convergence Time (min)
	During Rainfall				During Nonrainfall			
HKSL	1.77	0.83	2.59	38	1.35	0.86	1.71	34
HKWS	1.19	0.57	2.13	50.5	1.06	0.87	1.43	28

3.2. Accuracy Analysis of Real-Time PPP-Estimated ZTD

It can be seen from the previous section that the overall positioning accuracy of real-time multi-GNSS PPP was more stable, and the convergence speed was faster. Therefore, real-time PPP inversion ZTD used multi-GNSS for subsequent research. The real-time ZTD (PPP-ZTD) solved by CNES products was compared with the ZTD product released by IGS (IGS-ZTD) to evaluate its accuracy. IGS-ZTD is a postprocessing product generated by the IGS final orbit with a time resolution of 5 min and an accuracy of 5 mm as a reference [31]. The difference between the two groups of ZTD demonstrates the accuracy of PPP-ZTD. The HKSL and HKWS stations in Hong Kong are on the list of IGS continuous observation and tracking stations, so these two stations are selected for testing. Figure 4 shows the test results of the PPP-ZTD and IGS-ZTD time series and their differences between HKSL and HKWS stations during June 2021 (DOY 173-DOY 179, during rainfall periods) and August 2021 (DOY 229-DOY 235, during nonrainfall periods). The statistical results of the time series listed in Figure 4 are shown in Table 5. The RMS accuracy of PPP-ZTD at both stations during rainfall and nonrainfall periods was about 10 mm. This accuracy meets the 15 mm threshold required for the ZTD input accuracy of the NWP model used in meteorological applications [32].

Table 5. Bias, STDEV, and RMS between PPP-ZTD and IGS-ZTD.

Station	Bias (mm)	STDEV (mm)	RMS (mm)	Bias (mm)	STDEV (mm)	RMS (mm)
	During Rainfall			During Nonrainfall		
HKSL	5.43	9.14	10.52	2.1	9.72	9.91
HKWS	4.08	8.91	9.88	2.42	8.85	9.13

The ZTD calculated from ECMWF by the integration method at GPS stations was compared with GPS ZTD. The bias ranged from 11.5 to −28.6 mm with a corresponding average of −10.5 mm, while the largest RMS was 35.4 mm with an average of 24.3 mm [33]. It can be seen that the ZTD of NWP inversion had higher accuracy. Therefore, the ZTD reference values of other stations were considered to be replaced by NWP ZTD. It can be seen from Table 6 that the accuracy of real-time PPP-ZTD during nonrainfall periods was generally higher than that during rainfall periods. During nonrainfall periods, the RMS of real-time PPP-ZTD was about 10 mm, except for individual stations. The RMS of real-time PPP-ZTD was generally around 15 mm during rainfall.

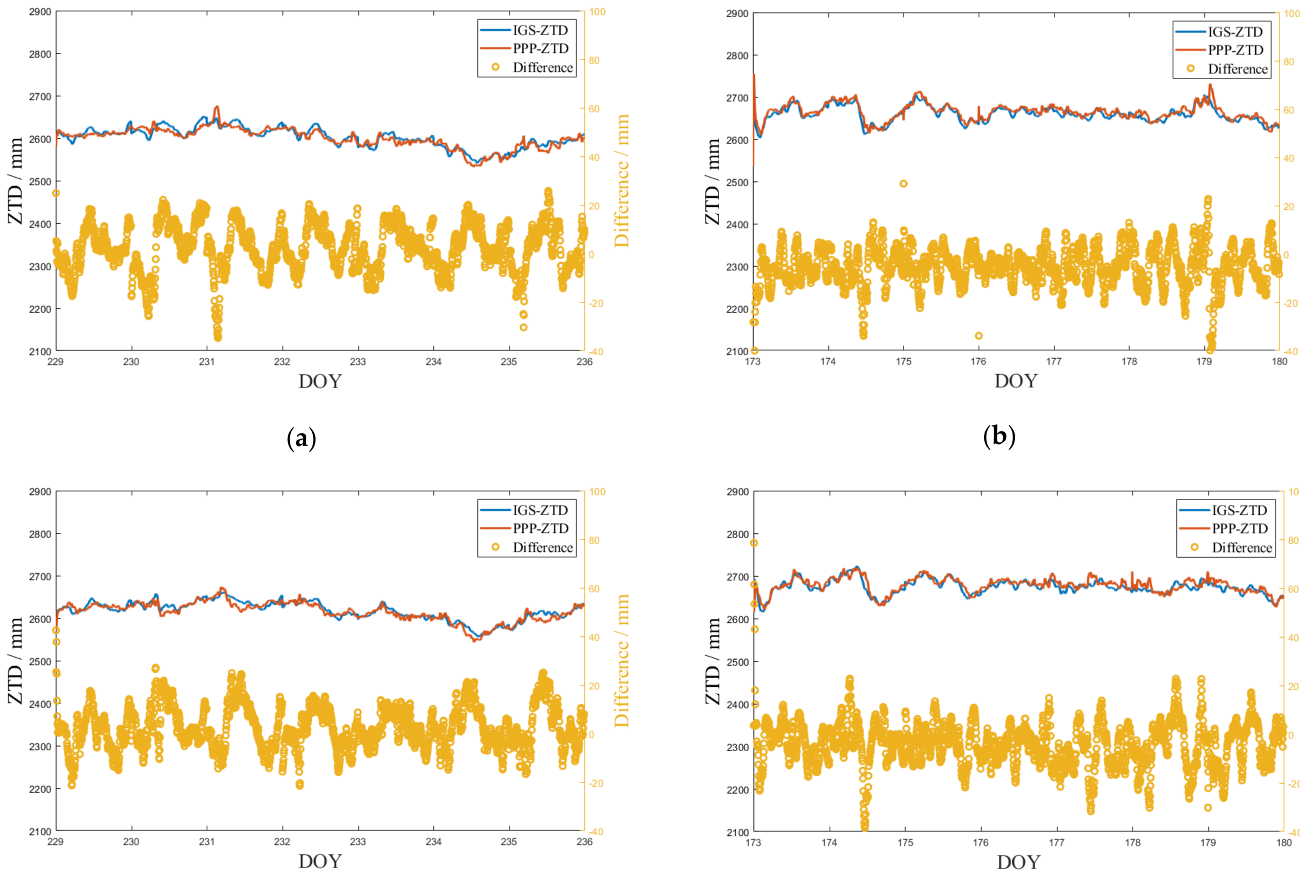

(**a**) (**b**)

(**c**) (**d**)

Figure 4. (**a**) Comparison of PPP-ZTD and IGS-ZTD at HKSL station during nonrainfall periods; (**b**) Comparison of PPP-ZTD and IGS-ZTD at HKSL station during rainfall; (**c**) Comparison of PPP-ZTD and IGS-ZTD at HKWS station during nonrainfall periods; (**d**) Comparison of PPP-ZTD and IGS-ZTD at HKWS station during rainfall.

Table 6. Bias, STDEV, and RMS between PPP-ZTD and NWP-ZTD.

Station	Bias (mm)	STDEV (mm)	RMS (mm)	Bias (mm)	STDEV (mm)	RMS (mm)
	During Rainfall			During Nonrainfall		
HKCL	12.02	18.24	15.47	8.84	14.57	11.42
HKFN	13.23	17.75	16.85	9.06	13.44	12.25
HKKS	12.24	20.65	15.86	9.32	14.35	12.07
HKKT	12.07	17.66	15.21	8.44	12.23	11.35
HKLM	10.74	18.64	14.15	9.08	15.91	11.36
HKLT	12.95	17.37	16.66	8.54	11.58	10.83
HKMW	15.66	18.65	19.14	14.29	11.05	17.24
HKNP	10.11	13.96	13.08	9.14	11.27	11.75
HKOH	15.25	19.37	18.67	9.26	11.16	11.56
HKPC	11.53	16.74	14.74	7.84	9.94	9.91
HKQT	14.17	22.36	17.95	8.36	12.83	10.82
HKSC	11.88	18.19	14.66	8.15	11.54	10.05
HKSS	13.02	18.74	16.74	8.55	13.01	11.35
HKST	12.64	16.55	15.55	8.64	10.83	10.92
HKTK	13.76	22.06	17.46	10.95	15.45	14.66
T430	13.12	17.83	16.97	9.06	12.81	12.24

3.3. Accuracy Analysis of Real-Time PPP PWV

In order to reflect the accuracy of real-time PPP PWV, this paper calculated the PWV of real-time PPP inversion (PPP PWV) according to the PWV formula calculated by ZTD in Section 2.2. Taking the PWV of the radiosonde station as a reference, the PPP PWV during June 2021 (DOY 173-DOY 179, during rainfall) and August 2021 (DOY 229-DOY 235, during nonrainfall) was evaluated [34]. Three stations near the radiosonde station were selected for comparative testing. Table 7 displays the statistical values of the average deviation, STDEV, and RMS of the HKSC station. Because the HKSC station was closest to the radiosonde station and the height difference was small, it was considered to be consistent. Therefore, taking the HKSC station as an example, the accuracy comparison of PPP PWV inversion between the HKSC station during rainfall and nonrainfall periods was drawn, as shown in Figures 5 and 6. During rainfall periods, except for DOY 176, there was rainfall on all days. As can be seen from Figures 5 and 6, the overall PWV during rainfall periods was higher than the PWV during nonrainfall periods. During rainfall periods, the PPP PWV of the HKSC station had a large deviation from the radiosonde station PWV (RS PWV), and the bias, STDEV, and RMS between the two sets of data were 3.45 mm, 1.79 mm, and 3.85 mm, respectively. During the nonrainfall period, the PPP PWV of the HKSC station and the PWV of the radiosonde station had good consistency between the two groups of data. The bias, STDEV, and RMS between the two groups of data were 0.93 mm, 1.21 mm, and 1.18 mm, respectively. The experimental results show that the accuracy of PPP PWV meets the requirements of the weather forecast and other related meteorological applications [35]. The large deviation in PPP PWV during rainfall may be due to the severe change in tropospheric delay over the station caused by weather changes [36].

Table 7. Bias, STDEV, and RMS between PPP PWV and radiosonde station PWV.

Station	Bias (mm)	STDEV (mm)	RMS (mm)	Bias (mm)	STDEV (mm)	RMS (mm)
	During Rainfall			During Nonrainfall		
HKSC	3.45	1.79	3.85	0.93	1.21	1.18

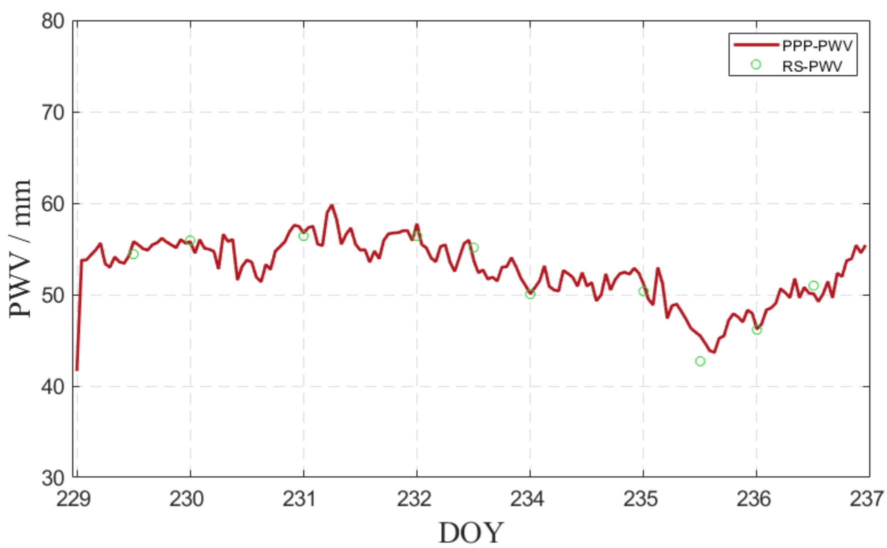

Figure 5. Comparison of PPP PWV between HKSC station and radiosonde station during nonrainfall.

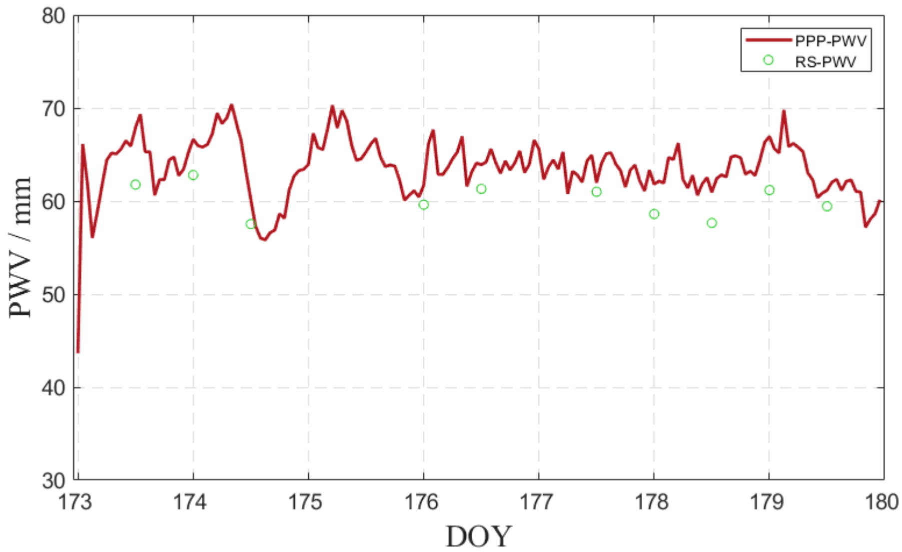

Figure 6. Comparison of PPP PWV between HKSC station and radiosonde station during rainfall.

The PWV retrieved through NWP (NWP PWV) is still used as the PWV reference value in other stations. It can be seen from Table 8 that during nonrainfall periods, the bias, STDEV, and RMS were generally lower than those during rainfall periods. In addition to individual sites, the RMS of real-time PPP PWV was below 2 mm when NWP PWV was used as a reference. The RMS of real-time PPP PWV was more than 2 mm during rainfall, and even more than 3 mm at some sites.

Table 8. Bias, STDEV, and RMS between PPP PWV and NWP PWV.

Station	Bias (mm)	STDEV (mm)	RMS (mm)	Bias (mm)	STDEV (mm)	RMS (mm)
	During Rainfall			During Nonrainfall		
HKCL	1.89	2.87	2.43	1.4	2.3	1.81
HKFN	2.09	2.79	2.65	1.42	2.12	1.93
HKKS	1.93	2.51	2.5	1.47	2.1	1.9
HKKT	1.93	3.25	2.5	1.47	2.27	1.9
HKLM	1.89	2.78	2.4	1.33	1.93	1.79
HKLT	1.7	2.93	2.22	1.42	2.53	1.78
HKMW	2.03	2.73	2.62	1.34	1.81	1.72
HKNP	2.45	2.93	3.01	2.24	1.74	2.71
HKOH	1.59	2.19	2.04	1.42	1.77	1.83
HKPC	2.39	3.04	2.92	1.45	1.76	1.82
HKQT	1.82	2.64	2.32	1.24	1.57	1.56
HKSL	2.23	3.52	2.84	1.32	2.03	1.71
HKSS	1.89	2.68	2.37	1.33	1.85	1.77
HKST	2.06	2.95	2.64	1.35	2.06	1.79
HKTK	1.97	2.59	2.44	1.36	1.7	1.72
HKWS	2.16	3.48	2.75	1.73	2.44	2.31
T430	2.21	3.05	2.79	1.53	1.89	2.04

4. Discussion

The comprehensive and systematic real-time monitoring of PWV changes is necessary to research and predict extreme weather [37]. In this paper, real-time PPP technology was used to study the change in PWV in real-time, and RS PWV was used as a reference to evaluate the accuracy of real-time PPP PWV during rainfall and nonrainfall periods. The experimental results show that compared with RS PWV, real-time PPP PWV and RS PWV have good consistency during nonrainfall periods. The bias, STDEV, and RMS between the two sets of data at the HKSC station within one week are 0.93 mm, 1.21 mm, and 1.18 mm, respectively. During rainfall periods, the bias, STDEV, and RMS between the two sets of data at the HKSC station within a week were 3.45 mm, 1.79 mm, and 3.85 mm, respectively. From the statistical results of Tables 6 and 8, it can be seen that when the ZTD and PWV inverted by the NWP model are used as a reference, the accuracy of ZTD inverted by real-time PPP and the accuracy of PWV inverted by real-time PPP are generally higher than those in rainfall periods. From Figures 5 and 6, it can be seen that the PWV during rainfall periods is higher than that during nonrainfall periods, and the PWV variation during rainfall periods is also higher than that during nonrainfall periods. The PWV change associated with DOY 174–175 during rainfall periods is the most significant. Studying the change in PWV with the change in precipitation and improving the accuracy of real-time PPP PWV during rainfall periods will be of great significance for the prediction of extreme weather.

5. Limitations and Future Direction of the Research

There are some limitations in this study. The first is the accuracy of CNES real-time orbit and clock products. If the accuracy of real-time orbit and clock products can be improved, the positioning accuracy of real-time PPP and the accuracy of water vapor inversion can be further improved. Secondly, in this study, the IF combination is used for the real-time PPP algorithm. Hong Kong is located in low latitudes. In low latitudes, the ionospheric content is higher than that in high latitudes. When the IF combination is adopted, it is difficult to eliminate the influence of the higher-order term of the ionospheric delay, which increases the convergence time of real-time PPP and has a certain impact on the positioning accuracy. In future research, higher-precision real-time orbit and clock products will be studied to improve the positioning performance of real-time PPP. A real-time PPP algorithm suitable for low-latitude areas is explored to avoid the influence of ionospheric delay on real-time PPP.

6. Conclusions

This paper uses HK CORS observation data and the multi-GNSS real-time orbit and clock products released by the CNES to realize multi-GNSS real-time PPP. Based on the ZTD products of IGS and the PWV data of the RS station and the ERA5 dataset, the positioning performance of real-time PPP during rainfall and nonrainfall periods and the accuracy of water vapor inversion are analyzed. The key results obtained from the current data suggest the following: (1) Compared with a single GPS system, real-time multi-GNSS PPP can reduce the convergence time of a single GPS system during both rainfall and nonrainfall periods. During nonrainfall periods, the convergence time of real-time multi-GNSS PPP is 12.06% less than that of single GPS systems. During rainfall periods, the convergence time of real-time multi-GNSS PPP is 29.20% less than that of single GPS systems. In terms of positioning accuracy, the multi-GNSS system has no obvious improvement effect on a single GPS system, and the average positioning accuracy in the E, N, and U directions under the two schemes is better than 3 cm. (2) Real-time PPP-ZTD experiments show that compared with IGS-ZTD, multi-GNSS real-time PPP-ZTD has higher accuracy. The accuracy of real-time PPP-ZTD during nonrainfall periods is higher than that during rainfall periods, whether using IGS-ZTD or NWP inversion ZTD as a reference. (3) The real-time PPP PWV experiment shows that the accuracy of real-time PPP PWV during nonrainfall periods is higher than that during rainfall periods, whether using RS PWV or NWP inversion PWV as a reference. The PWV value during rainfall periods is higher than that during nonrainfall periods.

Author Contributions: Conceptualization, Y.X., L.M. and F.Z.; methodology, L.M. and X.C.; software, L.M.; validation, Y.X., L.M. and X.C.; formal analysis, L.M.; investigation, L.M.; resources, Y.X.; data curation, L.M.; writing—original draft preparation, L.M., Y.X. and F.Z.; writing—review and editing, L.M.; visualization, L.M.; supervision, Y.X.; project administration, Y.X.; funding acquisition, Y.X. and Z.Y. All authors have read and agreed to the published version of the manuscript.

Funding: This research was funded by the National Natural Science Foundation of China (42174035) and the Talent Introduction Plan for the Youth Innovation Team in the Universities of Shandong Province (satellite position and navigation innovation team).

Informed Consent Statement: Not applicable.

Data Availability Statement: Not applicable.

Acknowledgments: We acknowledge the University of Wyoming, the International GNSS Service (IGS), the Hong Kong Geodetic Survey Services (HKGSS), the National Climate Data Center (NCDC), and the European Centre for Medium-Range Weather Forecasts (ECMWF) for providing relevant data and products.

Conflicts of Interest: The authors declare no conflict of interest.

References

1. Bevis, M.; Businger, S.; Herring, T.; Rocken, C.; Anthes, R.; Ware, R. GPS Meteorology: Remote sensing of atmospheric water vapor using the global positioning system. *J. Geophys. Res. Atmos.* **1992**, *97*, 15787–15801. [CrossRef]
2. Jin, S.G.; Luo, O.F. Variability and climatology of PWV from global 13-year GPS observations. *IEEE Trans. Geosci. Remote Sens.* **2009**, *47*, 1918–1924. [CrossRef]
3. Wang, J.H.; Zhang, L.Y.; Dai, A.G.; Hove, T.; Joel, V.B.; Wang, C. A near-global, 2-hourly data set of atmospheric precipitable water from ground-based GPS measurements. *J. Geophys. Res. Atmos.* **2007**, *112*, D11107. [CrossRef]
4. Zhang, H.X.; Yuan, Y.B.; Li, W.; Ou, J.; Li, Y.; Zhang, B.C. GPS PPP-derived precipitable water vapor retrieval based on Tm/Ps from multiple sources of meteorological datasets in China. *J. Geophys. Res. Atmos.* **2017**, *122*, 4165–4183. [CrossRef]
5. Bosy, J.; Rohm, W.; Borkowski, A.; Kroszczynski, K.; Figurski, M. Integration and verification of meteorological observations and NWP model data for the local GNSS tomography. *Atmos. Res.* **2009**, *96*, 522–530. [CrossRef]
6. Dai, A.G.; Wang, J.H.; Ware, R.; Van Hove, T. Diurnal variation in water vapor over North America and its sampling errors in radiosonde humidity. *J. Geophys. Res. Atmos.* **2002**, *107*, D10. [CrossRef]
7. Zhang, F.; Feng, P.; Xu, G.; Barriot, J.-P. Anomalous zenith total delays for an insular tropical location: The Tahiti Island case. *Remote Sens.* **2022**, *14*, 5723. [CrossRef]
8. Shi, J.B.; Xu, C.Q.; Guo, J.M.; Gao, Y. Real-time GPS precise point positioning-based precipitable water vapor estimation for rainfall monitoring and forecasting. *IEEE Trans. Geosci. Remote Sens.* **2015**, *53*, 3452–3459.
9. Zumberge, J.F.; Heflin, M.; Jefferson, D.C.; Watkins, M.; Webb, F. Precise point positioning for the efficient and robust analysis of GPS data from large networks. *J. Geophys. Res. Solid Earth* **1997**, *102*, 5005–5017. [CrossRef]
10. Li, X.X.; Ge, M.R.; Dai, X.L.; Ren, X.D.; Fritsche, M.; Schuh, H. Accuracy and reliability of multi-GNSS real-time precise positioning: GPS, GLONASS, Bei Dou, and Galileo. *J. Geod.* **2015**, *89*, 607–635. [CrossRef]
11. Cai, C.; Gao, Y.; Pan, L.; Zhu, J.J. Precise point positioning with quad-constellations: GPS, Bei Dou, GLONASS and Galileo. *Adv. Space Res.* **2015**, *56*, 133–143. [CrossRef]
12. Jin, S.; Wang, Q.; Dardanelli, G. A review on multi-GNSS for earth observation and emerging applications. *Remote Sens.* **2022**, *14*, 3930. [CrossRef]
13. Cai, C.; Gao, Y. Modeling and assessment of combined GPS/GLONASS precise point positioning. *GPS Solut.* **2013**, *17*, 223–236. [CrossRef]
14. Lou, Y.D.; Zheng, F.; Gu, S.F.; Wang, C.; Guo, H.L.; Feng, Y.M. Multi-GNSS precise point positioning with raw single-frequency and dual-frequency measurement models. *GPS Solut.* **2016**, *20*, 849–862. [CrossRef]
15. Liu, T.; Yuan, Y.B.; Zhang, B.C.; Wang, N.B.; Tan, B.F.; Chen, Y.C. Multi-GNSS precise point positioning (MGPPP) using raw observations. *J. Geod.* **2017**, *91*, 253–268. [CrossRef]
16. Li, X.X.; Dick, G.; Ge, M.R.; Heise, S.; Wickert, J.; Bender, M. Real-time GPS sensing of atmospheric water vapor: Precise point positioning with orbit, clock, and phase delay corrections. *Geophys. Res. Lett.* **2014**, *41*, 3615–3621. [CrossRef]
17. Yuan, Y.B.; Zhang, K.F.; Rohm, W.; Choy, S.; Robert, N.; Wang, C.S. Real-time retrieval of precipitable water vapor from GPS precise point positioning. *J. Geophys. Res. Atmos.* **2014**, *119*, 10043–10057. [CrossRef]
18. Lu, C.X.; Chen, X.H.; Liu, G.; Dick, G.; Wickert, J.; Jiang, X.Y.; Zheng, K.; Schuh, H. Real-Time tropospheric delays retrieved from multi-GNSS observations and IGS real-time product streams. *Remote Sens.* **2017**, *9*, 1317. [CrossRef]
19. Pan, L.; Guo, F. Real-time tropospheric delay retrieval with GPS, GLONASS, Galileo and BDS data. *Sci. Rep.* **2018**, *8*, 17067. [CrossRef]
20. Askne, J.; Nordius, H. Estimation of tropospheric delay for microwaves from surface weather data. *Radio Sci.* **1987**, *22*, 379–386. [CrossRef]
21. Gendt, G.; Dick, G.; Reigber, C.; Tomainiss, M.; Liu, Y.X.; Ramatschi, M. Near real time GPS water vapor monitoring for numerical weather prediction in germany. *J. Meteorol. Soc. Jpn.* **2004**, *82*, 361–370. [CrossRef]
22. Rocken, C.; Anthes, R.; Exner, M.; Hunt, D.; Sokolovskiy, S.; Ware, R.; Gorbunov, M.; Schreiner, W.; Feng, Y.; Herman, B.; et al. Analysis and validation of GPS/MET data in the neutral atmosphere. *J. Geophys. Res. Atmos.* **1997**, *102*, 29849–29866. [CrossRef]

23. Li, X.X.; Dick, G.; Lu, C.X.; Ge, M.R.; Nilsson, T.; Fritsche, M.; Wickert, J.; Schuh, H. Multi-GNSS Meteorology: Real-time retrieving of atmospheric water vapor from BeiDou, Galileo, GLONASS, and GPS observations. *IEEE Trans. Geosci. Remote Sens.* **2015**, *53*, 6385–6393. [CrossRef]
24. Dow, J.M.; Neilan, R.E.; Rizos, C. The international GNSS service in a changing landscape of global navigation satellite systems. *J. Geod.* **2009**, *83*, 191–198. [CrossRef]
25. Wang, M.; Chai, H.Z.; Xie, K.; Chen, Y.L. PWV inversion based on CNES real-time orbits and clocks. *J. Geod. Geodyn.* **2013**, *33*, 137–140.
26. Zhang, Q.; Ye, J.H.; Zhang, S.C.; Han, F. Precipitable water vapor retrieval and analysis by multiple data sources: Ground-based GNSS, radio occultation, radiosonde, microwave satellite, and NWP reanalysis data. *J. Sens.* **2018**, *2018*, 3428303. [CrossRef]
27. Byun, S.H.; Bar-Sever, Y.E.; Gendt, G. The new tropospheric product of the International GNSS Service. In Proceedings of the 18th International Technical Meeting of the Satellite Division of the Institute of Navigation (ION GNSS 2005), Long Beach, CA, USA, 13–16 September 2005; pp. 241–249.
28. Kouba, J.; Héroux, P. Precise point positioning using IGS orbit and clock products. *GPS Solut.* **2001**, *5*, 12–28. [CrossRef]
29. Boehm, J.; Heinkelmann, R.; Schuh, H. Short Note: A global model of pressure and temperature for geodetic applications. *J. Geod.* **2007**, *81*, 679–683. [CrossRef]
30. Bevis, M.; Businger, S.; Chiswell, S.; Herring, T.; Anthes, R.; Rocken, C.; Ware, R. GPS Meteorology: Mapping zenith wet delays onto precipitable water. *J. Appl. Meteorol.* **1994**, *33*, 379–386. [CrossRef]
31. Byun, S.H.; Bar-Sever, Y.E. A new type of troposphere zenith path delay product of the international GNSS service. *J. Geod.* **2009**, *83*, 1–7. [CrossRef]
32. De, H.S. *National/Regional Operational Procedures of GPS Water Vapour Networks and Agreed International Procedures*; WMO/TD-No. 1340; KNMI: De Bilt, The Netherlands, 2006; p. 20.
33. Chen, Q.; Song, S.; Stefan, H.; Liou, Y.H.; Zhu, W.; Zhao, J. Assessment of ZTD derived from ECMWF/NCEP data with GPS ZTD over china. *GPS Solut.* **2011**, *15*, 415–425. [CrossRef]
34. Park, C.G.; Baek, J.H.; Cho, J.H. Analysis on characteristics of radiosonde bias using GPS precipitable water vapor. *J. Astron. Space Sci.* **2010**, *27*, 213–220. [CrossRef]
35. Benevides, P.; Catalao, J.; Miranda, P. On the inclusion of GPS precipitable water vapour in the nowcasting of rainfall. *Nat. Hazards Earth Syst. Sci.* **2015**, *15*, 2605–2616. [CrossRef]
36. Xu, Y.; Chen, X.; Liu, M.; Wang, J.; Zhang, F.; Cui, J.; Zhou, H. Spatial-temporal relationship study between NWP PWV and precipitation: A case study of 'July 20′ heavy rainstorm in Zhengzhou. *Remote Sens.* **2022**, *14*, 3636. [CrossRef]
37. Zhao, L.; Cui, M.; Song, J. An improved strategy for real-time troposphere estimation and its application in the severe weather event monitoring. *Atmosphere* **2023**, *14*, 46. [CrossRef]